sustainability

MDPI

Article

Novel Long-Conjugated Backbone-Based Non-Fullerene Acceptors for Efficient and Eco-Friendly Ternary Organic Solar Cells

Sung Jae Jeon, Nam Gyu Yang and Doo Kyung Moon *

Nano and Information Materials (NIMs) Laboratory, Department of Chemical Engineering, Konkuk University, 120, Neungdong-ro, Gwawngjin-gu, Seoul 05029, Republic of Korea; always0529@nate.com (S.J.J.); chickabiddy@konkuk.ac.kr (N.G.Y.)

* Correspondence: dkmoon@konkuk.ac.kr; Tel.: +82-2-450-3498

Abstract: Organic solar cells (OSCs) are made from carbon-rich organic compounds with low environmental impacts, unlike the silicon in traditional solar panels. Some of these organic materials can be broken down and reprocessed, enabling the recovery of valuable components. Specifically, the active-layer materials that make up OSCs can be designed with sustainability in mind. However, it is important to note that practical active materials that can be used for the commercialization of OSCs are still an area of research and development due to their low efficiency/stability and processability. Herein, we designed and synthesized three A-D-A′-D-A-type long-conjugated non-fullerene acceptors (NFAs) by incorporating various electron-withdrawing groups into the benzothiadiazole-diindacenodithiophene core. These NFAs, by changing their end-capping groups, exhibit not only distinct physical, optical, and electrochemical properties, but also differences in crystallinity and exciton dissociation. As a result, they exhibited significant differences in photovoltaic performance in PM6 donor-based binary devices. The introduction of small amounts of NFAs as a third component in the PM6:BTP-eC9 blend significantly enhanced its photon harvesting capabilities and influenced its charge transfer dynamics. Finally, we achieved a remarkable power conversion efficiency of nearly 17% by utilizing an eco-friendly solvent. This study provides valuable insights for the development of NFAs in efficient and eco-friendly OSCs.

Keywords: organic solar cells; long-conjugated non-fullerene acceptors; ternary organic solar cells; eco-friendly solvent

Academic Editor: Shuhua Fang

Received: 15 December 2024
Revised: 4 January 2025
Accepted: 6 January 2025
Published: 10 January 2025

Citation: Jeon, S.J.; Yang, N.G.; Moon, D.K. Novel Long-Conjugated Backbone-Based Non-Fullerene Acceptors for Efficient and Eco-Friendly Ternary Organic Solar Cells. *Sustainability* **2025**, *17*, 512. https://doi.org/10.3390/su17020512

1. Introduction

As emerging photovoltaic (PV) technologies, dye-sensitized solar cells (DSSCs), organic solar cells (OSCs), and perovskite solar cells (PSCs) offer distinct advantages, including solution processibility, flexibility, lightweight components, and the ability to customize their design and geometry [1–3]. Among these technologies, OSCs emerge as promising candidates for building-integrated photovoltaic (BIPV)/automotive-integrated photovoltaic (AIPV) and indoor PV applications [2–4]. This potential is attributed to several unique advantages such as their high power conversion efficiencies (PCEs; >20% under incident light [5–10]; >30% under indoor light [11,12]), the inherent average visible transmittances of their photoactive materials (AVTs; >60%) [13], their fine-tunable spectral absorbance/frontier energy levels [13], and their low-cost/energy production

process [14]; hence, OSCs are regarded as potential renewable and sustainable energy resources for the near future.

However, OSCs continue to encounter significant challenges related to stability and sustainability. Their stability is consistently lower than that of conventional PVs, and environmentally sustainable manufacturing processes are often overlooked [4]. In particular, sustainability considerations will play a crucial role in the forthcoming commercialization of OSCs. Emphasis is placed on the utilization of non-toxic [15–17], readily available, and low-cost materials [1–3,13], which may include waste-derived and/or easily recyclable components [1,18].

Recently, Sun et al. proposed a novel approach that takes into account both stability and cost from the perspective of OSC recycling. They noted that if OSCs could be refurbished, their stability might become less prohibitive. Furthermore, the reuse of valuable OSC components could lead to a reduction in the price per watt of solar modules. The suggested OSC protocol has demonstrated the feasibility of recycling OSCs through a dismantling procedure that allows for the reuse of photoactive materials without incurring a performance loss. Additionally, this protocol facilitates the recovery of the silver (Ag) electrode and indium tin oxide (ITO) substrate through both chemical and physical processes. When combined with the developed physical mixing methodology, the OSCs fabricated from recycled components exhibit a performance comparable to that of newly manufactured devices. An analysis of their economic potential points out that this recycling protocol can save 14.24 USD m^2 in industrial scenarios. This report provides a significant guideline toward the cost-effective and high-yield recycling of waste OSCs [18].

Despite these technological advancements, an effective strategy for the development of photoactive materials that facilitate environmental sustainability, particularly in the context of roll-to-roll manufacturing for industrial applications, remains essential and may offer a viable solution for achieving truly sustainable OSCs. Based on the structure–property relationship of photoactive materials, several design strategies have been reported that emphasize an eco-friendly solvent process: e.g., for polymer donors, 3-fluoropyridine (FPy)-based terpolymer [17] and quaterpolymer approaches [13], and for non-fullerene acceptors (NFAs), long-branched alkyl side chains (2-decyltetradecyl, DT) [16] and oligo (ethylene glycol) (OEG) side chain substitutions [19].

In short, our research group designed and synthesized three polymer donors based on an asymmetric FPy, featuring a non-covalent conformation dual lock on one side and free torsion on the other. These polymers are intended for use in eco-friendly, solution-processable OSCs. Among the synthesized donor materials, the terpolymer PM6(FPy = 0.2), which incorporates 20% FPy units into the PM6 backbone, achieved its highest PCE of 16.1% when processed with eco-friendly toluene (17.0% when processed with toxic chloroform (CF)) with excellent reproducibility in BTP-eC9-based OSCs. Surprisingly, this polymer, characterized by its unique aggregation behavior, allows for precise tuning of the fibril network morphology of the polymer blend to the donor weight ratio. Based on this strategy, all OSCs demonstrated acceptably high PCEs ranging from 10.1% to 16.1%, while maintaining high fill factors (FFs) of over 72%, despite the proportion of polymer donors being decreased from 100% to 20%. Consequently, the optimized semitransparent OSCs (ST-OSCs) achieved high PCEs of 11.1% and 8.9% with AVTs of 32.6% and 41.1%, respectively, at donor-to-acceptor weight ratios of 0.5:1.0 of 0.25:1.0 [17].

In addition, from an industrialization perspective, our research group has designed and synthesized 12 novel cost-effective D–π = A polymer donors that have simultaneously high AVTs and coplanarity, facilitating the development of high-performance ST-OSCs. Among the synthesized donor materials, P(3IN = 0.3)(3IN2F = 0.5)(BDD = 0.2) is based on the quaterpolymer building block, which can reduce the regioregularity of polymer

backbones and increase the solubility of the polymer in eco-friendly solvents, such as TL and friendly *o*-xylene (XY). This quaterpolymer, when utilizing an XY-processed device incorporating BTP-eC9, achieved a maximum PCE of 14.0% along with high stability. Importantly, this blended film exhibited an AVT of 62.1% and a color rendering index of 95.0. Furthermore, a ternary device incorporating PM6 as a third component significantly enhances the PCE to 17.3%. Based on these advantages, binary and ternary ST-OSCs achieve light utilization efficiencies (LUEs) of 4.38% and 4.04%, respectively. Lastly, an air-processed, eco-friendly ternary ST-OSC module (active area: 4.7 cm^2) designed for indoor applications was integrated with a thermo-hygrometer, successfully creating a self-charging power source in real time under a 3000 K light-emitting diode light at 195 lx [13].

Dong et al. designed and synthesized an NFA designated as DTY6, which features long-branched alkyl chains (TD) attached to a central unit of dithienothiophene [3,2-b]-pyrrolobenzothiadiazole (TPBT), a typical Y6-core structure. The long-branched alkyl chains of DTY6 enhance solubility, facilitate its solvent-processing ability, and mitigate excessive molecular aggregation. Consequently, the PM6:DTY6-based device demonstrated a PCE of 16.1% when processed with the non-halogen solvent XY. Based on these results, XY-processed large-area OSC and ST-OSC modules (18 cm^2) were fabricated by blade coating and exhibited an outstanding PCE of 14.4% (certified to be 13.98% by a third-party accredited institute) and 11.6% (with an AVT of 10.8%), respectively [16].

Very recently, Zhang et al. developed a novel NFA designated as BTP-TO2, which incorporates an OEG side chain attached to the central nitrogen atom of the benzotriazole-based Y6 core. The OEG side chain ensures strong interactions between the small-molecule acceptor and its surrounding solvent molecules, without altering the conformation of the acceptor molecules across various solutions. BTP-TO2 yields comparable fine-active-layer morphologies when processed from a wide range of halogenated (CF and chlorobenzene (CB)) and non-halogenated solvents (TL and *p*-xylene), consistently contributing to high PCEs of approximately 19% and 16%, respectively, across all small-area OSC devices (0.062 cm^2) and large-area OSC modules (15.03 cm^2) incorporating PM6. They further generalized their morphological design rules based on the OEG side chains by developing additional NFAs, namely BTP-TO3 and ID-OEG-2F, which also demonstrate solvent-independent morphology and device performance [19].

Several studies have successfully rationally designed photoactive materials that are employed to fabricate highly efficient and eco-friendly solvent-processable OSCs; however, achieving a balance between efficiency and processability from a material perspective remains a significant challenge. Notably, selecting an appropriate solvent to dissolve relatively bulky active materials—considering factors such as boiling point and solubilizing power—along with optimizing the corresponding solvent-processed morphology of the photoactive layer, requires a deep understanding of molecular crystallinity and miscibility [13,17].

In this study, we design and synthesize three A-D-A′-D-A-type long-conjugated NFAs—**BT-dIDT-In**, **BT-dIDT-IC**, and **BT-dIDT-4Cl**—by incorporating various electron-withdrawing groups (EWGs), specifically indandione (In), indanone-dicyanomethylene (IC), and a four-chlorine-substituted IC (4Cl), into the benzothiadiazole-diindacenodithiophene (BT-dIDT) core. This core features eight sp^3 carbon-bridged hexyl phenyl side chains, which enhance solubility in common eco-friendly solvents [20]. These NFAs can provide highly planar backbones, which are derived from non-covalent conformational locking facilitated by S···O, S···N, and N···H interactions between adjacent units [17,21–24]. This structural arrangement leads to stretched S-shape curvatures with the longest conjugated length along the *x*-axis (L_x; >40 Å), which may

significantly influence the crystallinity and orientation characteristics of the material, as well as its stacking interactions with other materials [25–27].

Briefly, according to the change in EWGs, three NFAs (**BT-dIDT-In**, **BT-dIDT-IC**, and **BT-dIDT-4Cl**) showed different bandgaps (1.78 eV, 1.60 eV, and 1.51 eV) and highest occupied molecular orbital (HOMO) energy levels (−5.54 eV, −5.60 eV, and −5.67 eV), respectively. As a result, these NFAs showed a significant difference in their PCEs (0.04%, 2.82%, and 8.01%) when incorporated into binary devices with PM6. The introduction of small amounts of NFAs as a third component in the PM6:BTP-eC9 blend significantly enhanced their photon harvesting capabilities and influenced their charge transport properties. As a result, ternary OSCs incorporating **BT-dIDT-IC** and **BT-dIDT-4Cl** achieved enhanced PCEs of 16.73% and 16.63%, respectively, compared to that of a reference device (16.39%). For both ternary blends, we further fabricated devices that were processed with an eco-friendly solvent, XY, which resulted in improved PCEs of 16.45% and 16.84%, respectively, compared to that of the reference device (16.21%).

2. Materials and Methods

All details of the materials (poly(3,4-ethylenedioxythiophene):poly(styrenesulfonate) (PEDOT:PSS), poly[(2,6-(4,8-bis(5-(2-ethylhexyl-3-fluoro)thiophen-2-yl)-benzo[1,2-b:4,5-b′]dithiophene))-alt-(5,5-(1′,3′-di-2-thienyl-5′,7′-bis(2-ethylhexyl)benzo[1′,2′-c:4′,5′-c′] dithiophene-4,8-dione)] (PM6), 2,2′-((2Z,2′Z)-((12,13-bis(2-butyloctyl)-3,9-dinonyl-12,13-dihydro-[1,2,5]thiadiazolo[3,4-*e*]thieno[2″,3″:4′,5′]thieno[2′,3′:4,5]pyrrolo[3,2-*g*]thieno thieno[3,2-b]indole-2,10-diyl)bis(methanylylidene))bis(5,6-dichloro-3-oxo-2,3-dihydro-1H-indene-2,1-diylidene))dimalononitrile (BTP-eC9), 2,9-bis [3-[[3-(dimethylamino) propyl]amino]propyl]-anthra[2,1,9-*def*:6,5,10-*d′e′f′*]diisoquinoline-1,3,8,10(2H,9H)-tetrone (PDINN), etc.); instruments and characterization methods (proton nuclear magnetic resonance (^{1}H NMR), matric-assisted laser desorption ionization–time of flight (MALDI-TOF), thermogravimetric analysis (TGA), differential scanning calorimetry (DSC), ultraviolet–visible (UV–Vis) absorption and photoluminescence (PL), cyclic voltammetry (CV), two-dimensional grazing incidence wide-angle X-ray scattering (2D-GIWAXS), atomic force microscopy (AFM), density functional theory (DFT), etc.); device fabrication and characterization methods; space charge-limited-current (SCLC) measurements; and syntheses (2,2′-((benzo[c][1,2,5]thiadiazole-4,7-diylbis(4,4,9,9-tetrakis (4-hexylphenyl)-4,9-dihydro-s-indaceno[1,2-b:5,6-b′]dithiophene-7,2-diyl))bis(methanylylidene))bis(1H-indene-1,3(2H) -dione) (**BT-dIDT-In**), 2,2′-((2Z,2′Z)-((benzo[c][1,2,5]thiadiazole-4,7-diylbis(4,4,9,9-tetrakis (4-hexylphenyl)-4,9-dihydro-s-indaceno [1,2-b:5,6-b′]dithiophene-7,2-diyl))bis (methanylylidene)) bis(3-oxo-2,3-dihydro-1H-indene-2,1-diylidene))dimalononitrile (**BT-dIDT-IC**), 2,2′-((2Z,2′Z)-((benzo[c][1,2,5]thiadiazole-4,7-diylbis(4,4,9,9-tetrakis(4-hexylphenyl)-4,9 -dihydro-s-indaceno [1,2-b:5,6-b′]dithiophene-7,2-diyl))bis (methanylylidene))bis(5,6 -dichloro-3-oxo-2,3-dihydro-1H-indene-2,1-diylidene))dimalononitrile (**BT-dIDT-4Cl**)) can be found in the Supporting Information.

3. Results and Discussion

3.1. Molecular Synthesis and Thermal Properties

The synthetic routes of A-D-A′-D-A-type long-conjugated NFAs (**BT-dIDT-In**, **BT-dIDT-IC**, and **BT-dIDT-4Cl**) are shown in Scheme 1. Each product involves two synthetic steps. Initially, compound M1 was synthesized through Stille coupling [24], resulting in a yield of 84.1%. Subsequently, the compounds **BT-dIDT-In**, **BT-dIDT-IC**, and **BT-dIDT-4Cl** were synthesized from M1 using different EWGs (In, IC, and 4Cl) through Knoevenagel condensation [24,28] and were successfully collected in reasonable yields of 82.0%, 88.0%, and 87.0%, respectively. Detailed synthetic procedures and molecular characterizations (1H

NMR and MALDI-TOF) are provided in the Supporting Information (SI; Scheme S1 and Figures S1–S7).

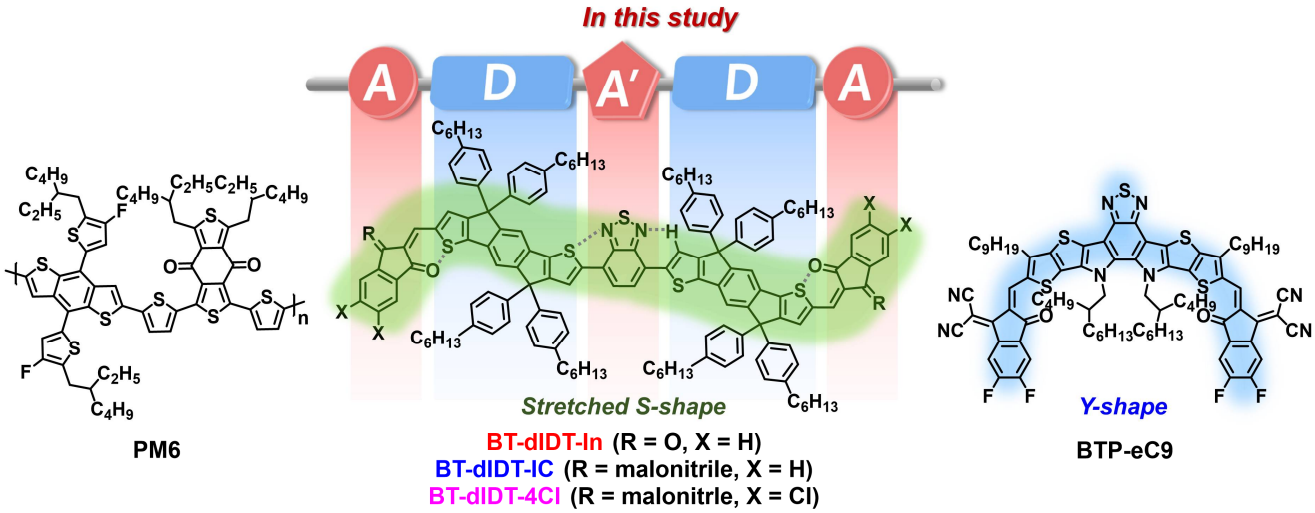

Scheme 1. Molecular structures of PM6, long-conjugated NFAs (**BT-dIDT-In**, **BT-dIDT-IC**, and **BT-dIDT-4Cl**, which have been developed in this study), and BTP-eC9.

The thermal properties of the NFAs were evaluated by TGA, as shown in Figure S8. **BT-dIDT-In** exhibits the highest decomposition temperature (T_d; 5% weight loss) of 422 °C, surpassing the 368 °C observed for **BT-dIDT-IC** and 340 °C observed for **BT-dIDT-4Cl**. This suggests that the removal of the dicyanomethylene groups from the IC and 4Cl units in **BT-dIDT-IC** and **BT-dIDT-4Cl**, respectively, contributes to an enhancement in thermal stability. Nevertheless, all NFAs have adequate thermal stability, exceeding 300 °C, which is essential for organic electronic applications [13,17,24,28].

To investigate the crystalline nature of the pure NFAs, DSC measurements were performed, the results of which are presented in the revised Supporting Information (Figure S9). Only two of the pure materials (**BT-dIDT-IC** and **BT-dIDT-4Cl**) exhibited inherent crystalline characteristics, as evidenced by their exothermal peaks during the heating process, in contrast to **BT-dIDT-In**. Specifically, **BT-dIDT-4Cl** exhibits two cold crystallization peaks ($T_{c,1}$ and $T_{c,2}$) at 217 °C and 283 °C, respectively, indicating the presence of two types of crystalline phases (probably due to polymorphism) [28]. In contrast, **BT-dIDT-IC** displays a single cold crystallization peak (T_c) at 247 °C. The total cold crystallization enthalpies for each material are nearly identical, with values of approximately 13 J/g. These results suggest that the crystalline nature increases in the sequence of **BT-dIDT-In**, **BT-dIDT-IC**, and **BT-dIDT-4Cl**.

3.2. Computational Simulations

Computational model compounds for **BT-dIDT-In**, **BT-dIDT-IC**, **BT-dIDT-4Cl**, BTP-eC9, and PM6 (with repeating units (n) set to n = 2) were generated by simplifying all alkyl chains to methyl groups to reduce computational time. DFT calculations were performed using the B3LYP/6-31(d) level of theory. Detailed DFT results of the optimized molecular geometries of all model compounds are summarized in Table S1. As illustrated in Figure 1, all three long-conjugated NFAs display highly planar molecular geometries, characterized by total dihedral angles (θ_{total}) that are approximately 0°. This planarity arises from non-covalent conformational locking facilitated by S···O, S···N, and N···H interactions between adjacent units [17,21–24]. This planar configuration is beneficial for electron delocalization [17,29]. The electron density of the HOMO and the lowest unoccupied

molecular orbitals (LUMOs) is uniformly distributed along the main conjugated backbones of A-D-A′-D-A-type NFAs.

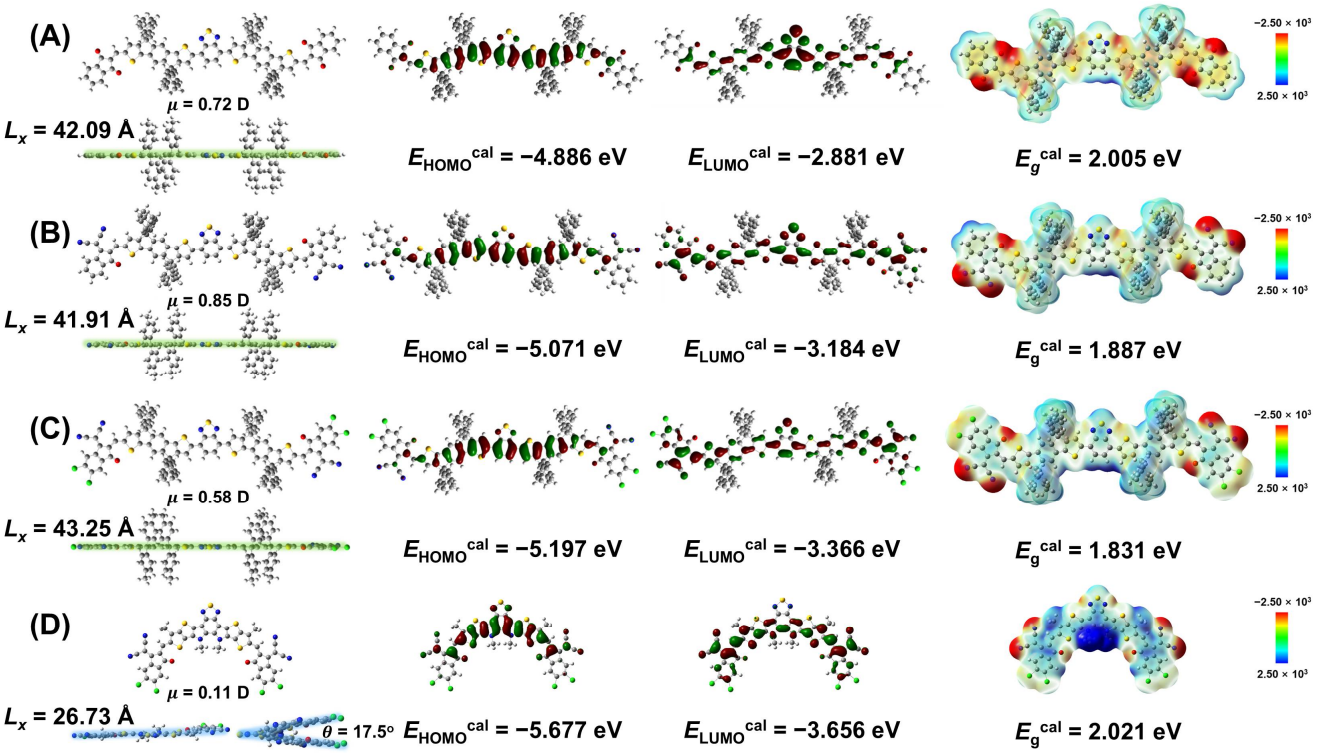

Figure 1. (**A**–**D**) DFT calculation results of the optimized geometries of the model compounds (**A**) **BT-dIDT-In**, (**B**) **BT-dIDT-IC**, (**C**) **BT-dIDT-4Cl**, and (**D**) BTP-ec9; top and side views (dipole moment (μ) and the longest conjugated length along the x-axis (L_x)), HOMO and LUMO electron clouds (HOMO and LUMO energy levels (E_{HOMO}^{cal} and E_{LUMO}^{cal}), and ESP surfaces (bandgap (E_g^{cal})) are presented in sequence.

Initially, to verify the curvature of the long-conjugated NFAs, a relaxed potential energy scan of the model compound BT-dIDT was performed, as shown in Figure S10. The results indicate that the stretched S-shaped geometry of BT-dIDT is the most favorable, as evidenced by the minimized energy state difference arising from intermolecular non-covalent interactions. The results are in good agreement with the findings reported in the references [22,23].

In contrast to the model compound of **BT-dIDT-In**, the model compounds of **BT-dIDT-IC** and **BT-dIDT-4Cl** exhibit significant delocalization within the IC and 4Cl units, respectively, as evidenced by their LUMO wave function distributions, which could contribute to the relatively low bandgaps in these compounds [30]. This trend is further supported by the variations in delocalization of the BT units within each LUMO electron cloud. These differences indicate that push–pull effects vary among the different EWGs, which can be attributed to the variations in their electron-withdrawing strengths [20,28]. Generally, to achieve an effectively low bandgap, the central group serves to push electrons, while the terminal groups work to pull them [21,24].

Therefore, the calculated bandgap (E_g^{cal}) values gradually decrease in the order of **BT-dIDT-In** (2.005 eV), **BT-dIDT-IC** (1.887 eV), and **BT-dIDT-4Cl** (1.831 eV) for each model compound. The calculated HOMO/LUMO energy levels (E_{HOMO}^{cal}/E_{LUMO}^{cal}) decrease in the same sequence of **BT-dIDT-In** (−4.886 eV/−2.396 eV), **BT-dIDT-IC** (−5.071 eV/−2.549 eV), and **BT-dIDT-4Cl** (−5.197 eV/−3.656 eV). The dipole moment (μ) values of the three long-conjugated NFAs are comparable, ranging from 0.58 to 0.85 D, and are relatively higher

than that of BTP-eC9 (0.11 D). Such elevated μ values may facilitate efficient intermolecular charge transfer and charge separation [24,29,31].

To gain a deeper understanding of their structure–property relationship, we conducted an analysis of the curvatures, L_x values, and electrostatic potential (ESP) surfaces of the model compounds, specifically long-conjugated NFAs and BTP-eC9. First, the molecular configurations of all long-conjugated NFAs exhibit similarly stretched S-shape curvatures, whereas BTP-eC9 shows a Y-shape curvature. Therefore, most NFAs, such as the Y6 analogs [32,33] and C-shaped NFAs [25,26], have a greater variety of intermolecular packing modes compared to straight/linear/S-shaped NFAs, which predominantly rely on end-group stacking due to the presence of bulky side chains on their core units [20,25,34,35]. In contrast, Y-shaped NFAs can facilitate various packing arrangements between their EWGs as well as their core units, due to their unique curvature and the presence of less bulky alkyl chains in their core unit, as reported in the literature [20]. Despite their limited inherent packing modes, long-conjugated NFAs exhibit higher L_x values, ranging from 41.91 Å to 43.25 Å, compared to that of BTP-eC9 (26.73 Å). Such large L_x values may affect the material's crystallinity and orientation, as well as its stacking interactions with other materials [25–27,34,35].

Next, it is noteworthy that the ESP surfaces of all the NFAs exhibit a partially stronger positive charge on the BT moiety, alongside a pronounced negative charge on the oxygen and nitrogen atoms of the flanked EWGs. However, this tendency is less pronounced in long-conjugated NFAs compared to that of BTP-eC9. Moreover, this trend becomes progressively weaker in the sequence of **BT-dIDT-4Cl**, **BT-dIDT-IC**, and **BT-dIDT-In**. Therefore, it can be anticipated that rapid charge transport in the order of BTP-eC9, **BT-dIDT-4Cl**, **BT-dIDT-IC**, and **BT-dIDT-In** may occur within the conjugated backbone due to electrostatic forces when blended with PM6 (Figure S13) [24].

3.3. Optical and Electrochemical Properties, Photovoltaic Performance, and Charge Transport Properties

The molar absorption coefficients ($\boldsymbol{\varepsilon_{sol}}$) of the long-conjugated NFAs in their CF solution state are presented in Figure S12. As a result, the maximum $\boldsymbol{\varepsilon_{sol}}$ values of **BT-dIDT-In**, **BT-dIDT-IC**, and **BT-dIDT-4Cl** were found to be 1.58×10^5 M^{-1} cm^{-1}, 1.64×10^5 M^{-1} cm^{-1}, and 1.74×10^5 M^{-1} cm^{-1}, respectively, which are similar to or slightly higher than those of high-performance NFAs reported in the literature [36–38]. These values exhibited an increasing trend with the substitution of EWGs from In to IC units and then to 4Cl units. As shown in Figure S12 and Figure 2A, the long-conjugated NFA values of **BT-dIDT-In**, **BT-dIDT-IC**, and **BT-dIDT-4Cl** exhibited significant redshifts in their absorption spectra in their film state, with maximum absorption wavelengths of 87.6 nm, 79.7 nm, and 83.3 nm, respectively. As a result, the optical bandgap (E_g^{opt}) values of **BT-dIDT-In**, **BT-dIDT-IC**, and **BT-dIDT-4Cl** were determined to be 1.78 eV, 1.60 eV, and 1.51 eV, respectively, which agree with the trend observed in the DFT calculation results. With the exception of **BT-dIDT-In**, both **BT-dIDT-IC** and **BT-dIDT-4Cl** demonstrated complementary absorption spectra when combined with PM6 and/or the PM6:BTP-eC9 blend. This complementary behavior represents a favorable strategy for enhancing these materials' light harvesting properties by fabricating binary and/or ternary OSCs.

The frontier energy levels of long-conjugated NFAs were determined using cyclic voltammetry (CV), as shown in Figure 2B. As a result, the HOMO/LUMO levels (E_{HOMO}/E_{LUMO}) of **BT-dIDT-In**, **BT-dIDT-IC**, and **BT-dIDT-4Cl** were found to be −5.54 eV/−3.76 eV, −5.60 eV/−4.00 eV, and −4.16 eV/−5.67 eV, respectively. This trend is in agreement with the results obtained from DFT calculations. As shown in Figure 2C, it was anticipated that only **BT-dIDT-4Cl** among the long-conjugated NFAs would exhibit favorable HOMO level alignments with both PM6 and BTP-eC9, thereby promoting effi-

cient charge transport [24,38]. However, for the PM6:**BT-dIDT-In** and PM6:**BT-dIDT-IC** combinations, the HOMO offsets would be reversed, measuring −0.08 eV and −0.02 eV, respectively. Nevertheless, the open-circuit voltage (V_{OC}), when blended with PM6, can be expected to increase in the following order: **BT-dIDT-In**, **BT-dIDT-IC**, and **BT-dIDT-4Cl**. The optical and electrochemical parameters of long-conjugated NFAs, as well as PM6 and BTP-eC9, are presented in Tables 1 and S2.

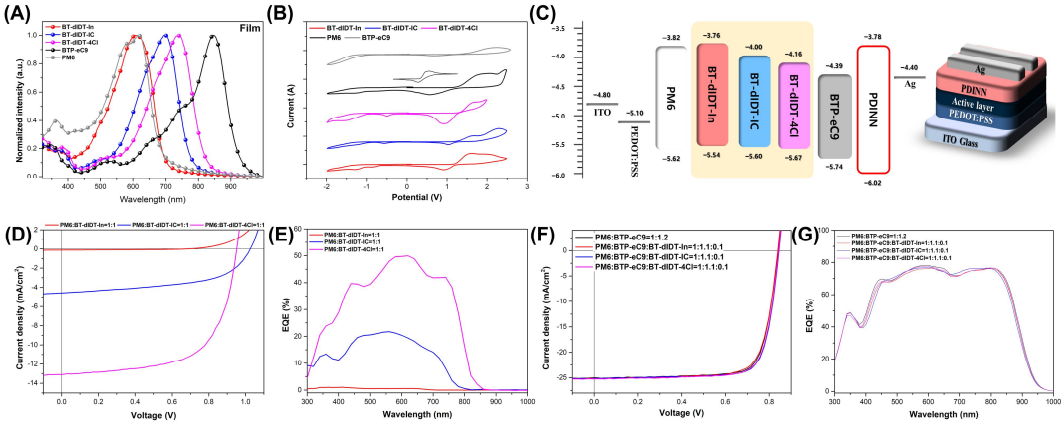

Figure 2. (**A**) Normalized absorption spectra, (**B**) CV curves, and (**C**) energy band diagrams (including the device configuration) of the photoactive materials (**BT-dIDT-In**, **BT-dIDT-IC**, **BT-dIDT-4Cl**, PM6, and BTP-eC9). (**D**,**F**) *J*–*V* and (**E**,**G**) EQE curves of optimized binary and ternary OSCs based on long-conjugated NFAs (**BT-dIDT-In**, **BT-dIDT-IC**, and **BT-dIDT-4Cl**).

Table 1. Optical and electrochemical properties of long-conjugated NFAs (**BT-dIDT-In**, **BT-dIDT-IC**, and **BT-dIDT-4Cl**).

	λ_{max}^{sol} [nm]	ε_{sol} [1] [10^5 M^{-1} cm^{-1}]	λ_{max}^{film} [nm]	λ_{onset}^{film} [nm]	E_g^{opt} [2] [eV]	E_{ox}^{onset} [V]	E_{HOMO} [3] [eV]	E_{LUMO} [4] [eV]
BT-dIDT-In	597.5	1.58	608.7	696.3	1.78	1.18	−5.54	−3.76
BT-dIDT-IC	676.6	1.64	695.8	775.5	1.60	1.24	−5.60	−4.00
BT-dIDT-4Cl	702.5	1.74	737.9	821.2	1.51	1.31	−5.67	−4.16

[1] The molar absorption coefficient was calculated using the Beer−Lambert law for four diluted solutions with varying concentrations to the order of 10^5 M; [2] E_g^{opt} = 1240/λ_{onset}^{film} (λ_{onset}^{film}s were calculated from the intersection of the tangent of the low energetic edge of the absorption spectrum with the baseline); [3] E_{HOMO} = −4.8 − [E_{ox}^{onset} (vs. Ag/AgCl) − $E_{1/2}$(Fc/Fc^+ vs. Ag/AgCl)] ($E_{1/2}$(Fc/Fc^+ vs. Ag/AgCl) = 0.44 eV); [4] E_{LUMO} = E_g^{opt} + E_{HOMO}.

The photovoltaic characteristics of three long-conjugated NFAs were investigated using the conventional device of ITO/PEDOT:PSS/PM6:long-conjugated NFA/PDINN/Ag, as illustrated in Figure 2C. All binary blends of PM6 and long-conjugated NFAs (1:1 wt%) were prepared in CB (0.5 vol% 1,8-diiodooctane (DIO)) solutions, and the corresponding binary devices were optimized. The *J*–*V* and external quantum efficiency (EQE) curves of the optimized binary OSCs are presented in Figures 2D and 2E, respectively. Among the binary OSCs, the device based on the PM6:**BT-dIDT-4Cl** blend exhibited the highest PCE of 8.01%, with a V_{OC} of 0.960 V, a short-circuit current density (J_{SC}) of 12.7 mA/cm^2, and an FF of 65.7%, which is much higher than the PCEs of OSCs based on the PM6:**BT-dIDT-IC** (2.82%) and PM6:**BT-dIDT-In** (0.04%) blends. The fabricated binary OSCs exhibited poor reliability, as evidenced by the comparison between J_{SC} and the calculated J_{SC} (J_{SC}^{cal}). This observation may be attributed to the instability of the device, which exhibits relatively poor performance in real time under ambient conditions. These results are in good agreement with the energy loss (E_{loss}) values observed for PM6:**BT-dIDT-4Cl** (0.543 eV), PM6:**BT-dIDT-IC** (0.591 eV), and PM6:**BT-dIDT-In** (1.091 eV) OSCs. It is evident that the differences in

frontier energy levels between the binary blends significantly influence device performance, as reported in the literature [24,28].

As shown in Figure S13 and Table S3, the charge transfer properties between PM6 and long-conjugated NFAs were examined through PL analysis. Briefly, the PM6 donor film exhibited a pronounced PL emission in the range of 600 to 850 nm when excited at 530 nm. Based on this phenomenon, the PL quenching rates ($PLQ_{D\rightarrow B}$) of all binary blends were calculated by determining the difference in PL emissions between the donor and the blend. As a result, the $PLQ_{D\rightarrow B}$ values of PM6:**BT-dIDT-4Cl**, PM6:**BT-dIDT-IC**, and PM6:**BT-dIDT-In** blend films were found to be 87.0%, 78.0%, and 51.0%, respectively. This trend is consistent with the observed order of their photovoltaic performance. These results can be attributed to the differences in their HOMO and LUMO energy offsets [20,24,28,39]. As shown in Figure 2C and Table S3, the PM6:**BT-dIDT-4Cl** blend demonstrated a minimized HOMO energy offset of 0.05 eV and an appropriate LUMO energy offset of 0.34 eV. In contrast, the PM6:**BT-dIDT-IC** blend exhibited a reversed HOMO energy offset of −0.02 eV. Furthermore, the PM6:**BT-dIDT-In** blend showed both reversed HOMO and LUMO energy offsets of −0.08 eV and −0.06 eV, respectively. These findings suggest that the reversed HOMO and/or LUMO offsets between the donor and acceptor can induce charge recombination processes such as "back hole transfer" and/or "back electron transfer" [24,39].

To verify the potential of long-conjugated NFAs, ternary OSCs were further fabricated using CF (0.5 vol% DIO) solutions, as illustrated in Figure 2F,G. The reference device based on the PM6:BTP-eC9 (1:1.2 wt%) blend exhibited an acceptable PCE of 16.39%, with a V_{OC} of 0.838 V, a J_{SC} of 25.0 mA/cm^2, and an FF of 78.2%. All ternary OSCs were optimized using a PM6:BTP-eC9:long-conjugated NFA (1:1.1:0.1 wt%) composition. In short, the introduction of small amounts of **BT-dIDT-IC** and **BT-dIDT-4Cl** into the PM6:BTP-ec9 blend resulted in improved PCEs of 16.73% and 16.63%, respectively, compared to the reference device. These results can be attributed to the enhancements observed in both FF and J_{SC} values. In contrast, the **BT-dIDT-In**-based ternary device exhibited a lower PCE of 16.12% than the reference device, primarily due to a reduced FF of 76.6%. This decrease in FF may be attributed to inadequate energy level alignments among the active materials derived from **BT-dIDT-In** [24,39]. All ternary OSCs exhibited similar E_{loss} values of approximately 0.48 eV, regardless of the specific third components used. All devices demonstrated high reliability, with deviations in J_{SC} and $J_{SC}{}^{cal}$ values remaining within 5%.

As shown in Figure S14 and Table S4, the charge transfer properties of all ternary blends were investigated, employing the same methodology as the binary blends described above. To ensure a thorough analysis, the PM6 donor films were examined under excitation at 530 nm and 630 nm, respectively, and the results were cross-checked. In short, only the ternary blend based on the **BT-dIDT-IC** exhibited higher $PLQ_{D\rightarrow B}$ values of 75.0% and 80.0%, respectively, when excited both at 530 nm and 630 nm, compared to the reference PM6:BTP-ec9 blend (73.0% and 78.0%). In contrast, the **BT-dIDT-In**-based ternary blend showed the lowest $PLQ_{D\rightarrow B}$ values (61.0% and 68.0%), which is consistent with the results for the binary blends, as discussed above. However, for the **BT-dIDT-4Cl**-based ternary blend, the $PLQ_{D\rightarrow B}$ values were similar to the reference blend. This result is perplexing, as the alignment of HOMO and LUMO levels among the three active materials represents the optimal configuration within ternary blends, as demonstrated by the energy offset values presented in Table S4.

To gain a better understanding of the photovoltaic performance of ternary OSCs, we fabricated electron-only and hole-only devices, which were evaluated by the SCLC method, as illustrated in Figure S15. Their charge carrier mobility values were determined using the modified Mott–Gurney equation and the relevant parameters are summarized in Table S5. Briefly, the BT-dIDT-4Cl-based ternary blend exhibited enhanced electron (μ_e) and hole (μ_h)

mobilities of 8.9×10^4 cm^2 V^{-1} s^{-1} and 2.0×10^3 cm^2 V^{-1} s^{-1}, respectively, in comparison to the reference binary blend (6.7×10^4 cm^2 V^{-1} s^{-1} and 1.6×10^3 cm^2 V^{-1} s^{-1}). The μ_e and μ_h values of the other ternary blends were observed to decrease in the sequence of **BT-dIDT-IC** and then **BT-dIDT-In**, compared to the reference binary blend. Furthermore, the balance μ_e/μ_h ratio values decreased sequentially to 0.55, 0.44, 0.42, and 0.39 for the PM6:BTP-eC9:**BT-dIDT-IC**, PM6:BTP-eC9:**BT-dIDT-4Cl**, PM6:BTP-eC9, and PM6:BTP-eC9:**BT-dIDT-In** blends, respectively. These results are consistent with the photovoltaic performances discussed above, particularly regarding the trends in FF values. All photovoltaic parameters of the optimized binary and ternary OSCs are summarized in Table 2.

Table 2. Photovoltaic parameters of optimized binary and ternary OSCs based on long-conjugated NFAs (**BT-dIDT-In**, **BT-dIDT-IC**, and **BT-dIDT-4Cl**).

Photoactive Layer Condition	V_{OC} [V]	J_{SC} [mA/cm^2]	J_{SC}^{cal} [mA/cm^2]	FF [%]	PCE_{max} (PCE_{ave} [1]) [%]	E_{loss} [2] [eV]
PM6:**BT-dIDT-In** = 1:1	0.682	0.13	0.12	40.9	0.04 (0.03 ± 0.01)	1.091
PM6:**BT-dIDT-IC** = 1:1	1.000	4.8	3.82	58.7	2.82 (2.65 ± 0.15)	0.591
PM6:**BT-dIDT-4Cl** = 1:1	0.960	12.7	10.79	65.7	8.01 (7.86 ± 0.15)	0.543
PM6:BTP-eC9 = 1:1.2	0.838	25.0	23.89	78.2	16.39 (16.30 ± 0.05)	0.481
PM6:BTP-eC9:**BT-dIDT-In** = 1:1.1:0.1	0.838	25.1	23.87	76.6	16.12 (15.97 ± 0.11)	0.482
PM6:BTP-eC9:**BT-dIDT-IC** = 1:1.1:0.1	0.838	25.2	23.94	79.2	16.73 (16.56 ± 0.16)	0.485
PM6:BTP-eC9:**BT-dIDT-4Cl** = 1:1.1:0.1	0.838	25.3	24.08	78.4	16.63 (16.56 ± 0.05)	0.482

[1] Average parameters with standard deviation obtained from 10 individual devices; [2] E_{loss} can be estimated by the equation $E_{loss} = E_g^{opt} - eV_{OC}$, where E_g^{opt} is the smallest optical bandgap between the donor and acceptor, extracted from the EQE curve.

3.4. Crystallinity and Orientation Properties

2D-GIWAS measurements were further employed to investigate the molecular crystallinity and orientation of neat films. The 2D-GIWAXS of all photoactive materials were obtained, as illustrated in Figure 3A–E. The corresponding 1D profiles in the out-of-plane (OOP) and in-plane (IP) directions are shown in Figure 3F. Additionally, the intensity-integrated azimuthal pole figure plots for the (100) scattering peaks are illustrated in Figure 3G. The (100) and (010) distances ($d_{(100)}$ and $d_{(010)}$) were calculated using Bragg's law. The (100) and (010) crystal coherence lengths ($CCL_{(100)}$ and $CCL_{(010)}$) were determined from the full width at half maximum (FWHM) values using the Scherrer equation. The integrated areas within the azimuthal angle ranges of 0–45° (A_z^1) and 90–135° (A_z^2), as well as 45–90° (A_{xy}^1) and 90–180° (A_{xy}^2), are defined as the corresponding fractions of face-on and edge-on structures, respectively; thus, the face-on to edge-on ratio (A_{xy}/A_z) was calculated as an average for both the 0–90° and 90–180° regions. The relevant parameters of the detailed 2D-GIWAXS analysis are summarized in Table S6 and are primarily derived from the OOP directions.

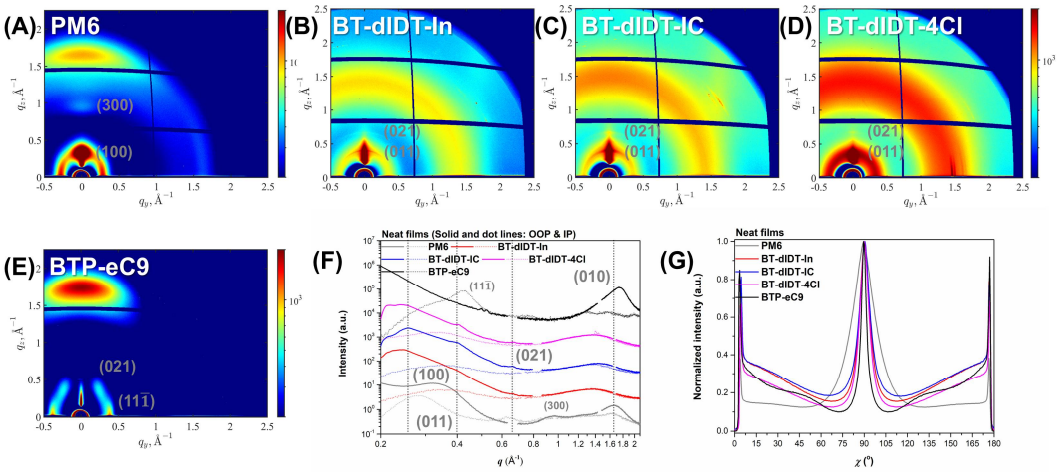

Figure 3. (**A**–**E**) 2D-GIWAXS pattern images of neat films based on (**A**) PM6, (**B**) **BT-dIDT-In**, (**C**) **BT-dIDT-IC**, (**D**) **BT-dIDT-4Cl**, and (**E**) BTP-eC9. (**F**) The corresponding 1D profiles in the out-of-plane (OOP; solid line) and in-plane (IP; dot line) directions. (**G**) The corresponding azimuthal pole figures extracted from the 0–180° of the (100) lamellar diffraction.

In terms of the PM6 donor polymer, it can be observed that the film predominantly adopts an edge-on orientation, as evidenced by its A_{xy}/A_z value of 0.42. Additionally, the PM6 film exhibited three diffraction peaks corresponding to the (100), (300), and (010) planes in the OOP direction, which are typical characteristics of PM6 as reported in the literature [13]. As for the BTP-eC9 film, two diffraction peaks were observed: one (11$\bar{1}$) at 0.424 Å^{-1} in the IP direction and another (010) at 1.744 Å^{-1} in the OOP direction [8,10,33]. This finding indicates that BTP-ec9 exhibits a face-on dominant orientation, which is further corroborated by its A_{xy}/A_z value of 1.40.

In contrast to the distinct packing behaviors of PM6 and BTP-eC9, all long-conjugated NFAs exhibited relatively poor orientation and crystallinity. Nevertheless, long-conjugated NFAs display several distinctive crystalline features in the OOP direction, characterized by three diffraction peaks located at approximately 0.24–0.26 Å^{-1}, 0.38–0.40 Å^{-1}, and 0.65–0.66 Å^{-1}. These peaks may be attributed to the (100), (011), and (021) planes, respectively, as estimated in the literature [8,32,33,40]. Among the three long-conjugated NFAs, regarding their (010) plane properties, the **BT-dIDT-IC** film exhibits the shortest $d_{(100)}$ value of 24.53 Å, whereas the **BT-dIDT-4Cl** film shows the largest $CCL_{(100)}$ value of 67.82 Å. For both the (011) and (021) planes, it is challenging to ascertain precise values due to their indistinct peaks relative to the baseline. However, some trends can be observed: the (011) and (021) distance values decrease in the order of **BT-dIDT-In**, **BT-dIDT-IC**, and **BT-dIDT-4Cl**, while the (011) and (021) CCL values increase in the same order. Lastly, all long-conjugated NFAs exhibited distinctly amorphous rings [24,41], located at approximately 1.36–1.44 Å^{-1} in the OOP direction, as illustrated in Figure 3B–D. This finding suggests that variations in the EWGs do not significantly influence their π–π stacking interactions.

As shown in Figure 4, 2D-GIWAXS measurements of long-conjugated NFA-based ternary blend films were conducted to understand the correlation between molecular packing properties and device performance, employing the same methodology as used for the neat films described above. The relevant parameters for detailed 2D-GIWAXS analyses are summarized in Table S7. The (010) and (010) relevant parameters are derived from the IP and OOP directions, respectively. As shown in Figure 4A–E, the PM6:BTP-eC9 blend (reference binary device) exhibits the most pronounced face-on orientation when compared to the three ternary blends, as evidenced by the highest A_{xy}/A_z value of 1.49. Nevertheless, all ternary blends exhibited reasonable A_{xy}/A_z values ranging from 1.08 to 1.16, which are

slightly lower than that of the reference film. However, for the $d_{(100)}$ and $CCL_{(100)}$ values, the **BT-dIDT-IC**-based ternary blend film, which had the best performance among the devices, exhibits superior values of 20.97 Å and 58.54 Å, respectively, when compared to the other films. In contrast, for its $d_{(100)}$ and $CCL_{(100)}$ values, the **BT-dIDT-4Cl**-based ternary blend film shows notable values of 3.666 Å and 31.00 Å, respectively, in comparison to the other films. Comprehensively, the films' lamellar packing properties increase in the following order: PM6:BTP-eC9:**BT-dIDT-In**, PM6:BTP-eC9 ≈ PM6:BTP-eC9:**BT-dIDT-4Cl**, and PM6:BTP-eC9:**BT-dIDT-IC** blends. Similarly, their π–π stacking properties increase in the following order: PM6:BTP-eC9:**BT-dIDT-In**, PM6:BTP-eC9, PM6:BTP-eC9:**BT-dIDT-IC**, and PM6:BTP-eC9:**BT-dIDT-4Cl**, blends. These trends are consistent with the photovoltaic results, as evidenced by the relevant values discussed above.

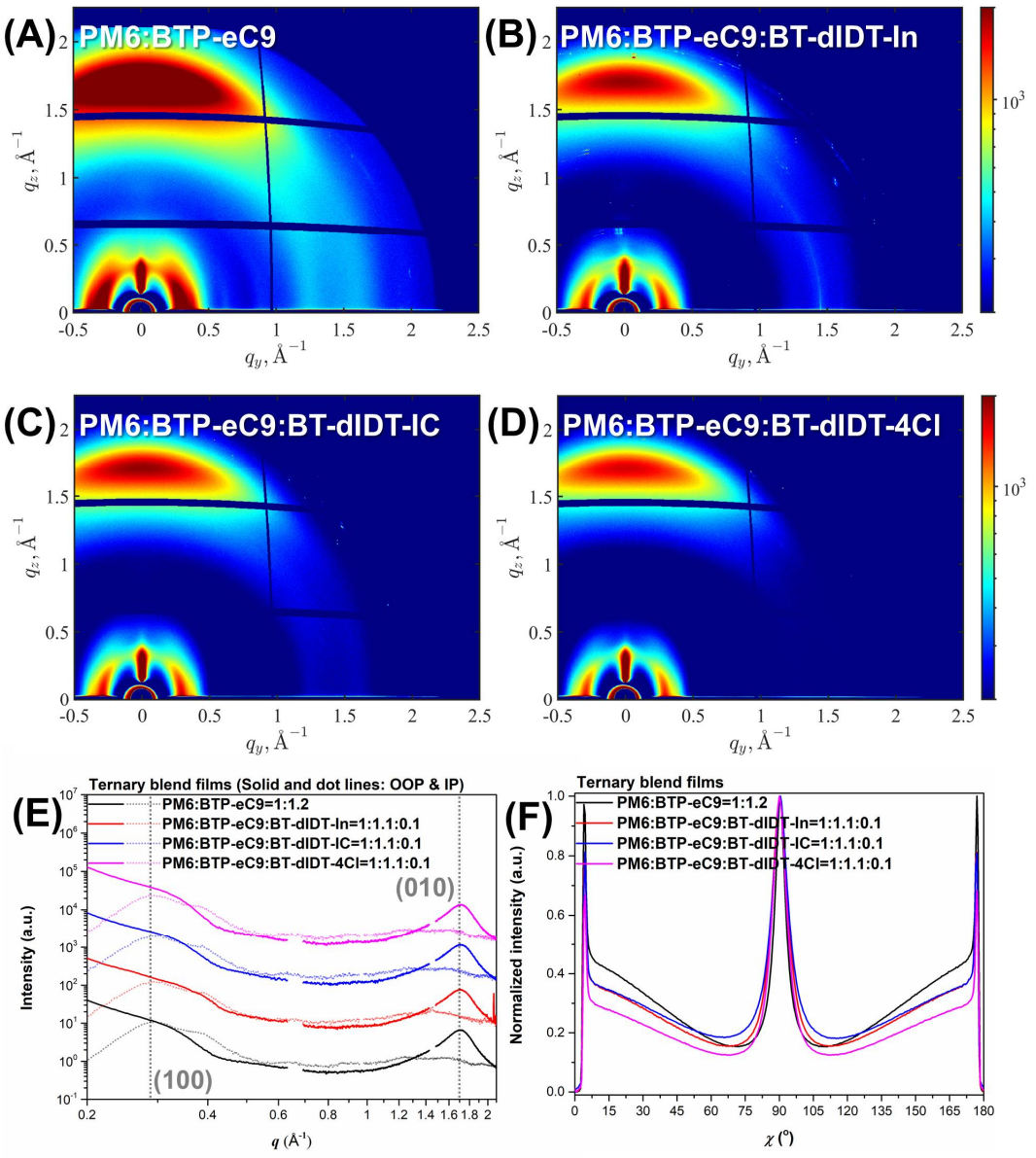

Figure 4. (**A**–**D**) 2D-GIWAXS pattern images of optimized ternary blends based on (**A**) PM6:BTP-eC9 = 1:1.2, (**B**) PM6:BTP-eC9:**BT-dIDT-In** = 1:1.1:0.1, (**C**) PM6:BTP-eC9:**BT-dIDT-IC** = 1:1.1:0.1, and (**D**) PM6:BTP-eC9:**BT-dIDT-4Cl** = 1:1.1:0.1. (**E**) The corresponding 1D profiles in the OOP and IP (Solid and dot lines) directions. (**F**) The corresponding azimuthal pole figures extracted from 0–180° of the (100) lamellar diffraction.

3.5. Morphological Properties

AFM measurements were conducted to investigate the surface morphologies of long-conjugated NFA-based ternary blend films, as depicted in Figure 5. The reference binary blend film (PM6:BTP-ec9) showed a homogeneous surface with a root mean square (RMS) roughness value of 1.18 nm, which implies well-mixed D-A interpenetrating networks [36,37]. In contrast, the **BT-dIDT-In**-based ternary blend film, which demonstrated the best performance, exhibited a relatively smooth surface with a reduced RMS value of 1.12 nm [17], which is the lowest among the four blend films evaluated. Furthermore, it is evident that the large aggregates are significantly minimized, leading to a reduction in charge recombination and ultimately resulting in the highest FF observed among the devices [17,24,32]. In contrast, the ternary films incorporating **BT-dIDT-In** and **BT-dIDT-4Cl** exhibited relatively large-scale and bicontinous phase separation [16]. These morphologies can contribute to efficient charge transport, thereby leading to an increase in the J_{SC} and FF values of the device [25]. However, when the domain sizes are excessively large, they may facilitate charge recombination [26,32]. Nevertheless, we speculate that the morphology of the **BT-dIDT-4Cl**-based ternary blend film is superior to that of the **BT-dIDT-In**-based ternary blend film, as evidenced by its lower RMS value of 1.18 nm, which is equivalent to that of the PM6:BTP-eC9 blend film. These observations provide support for the photovoltaic performance results presented above.

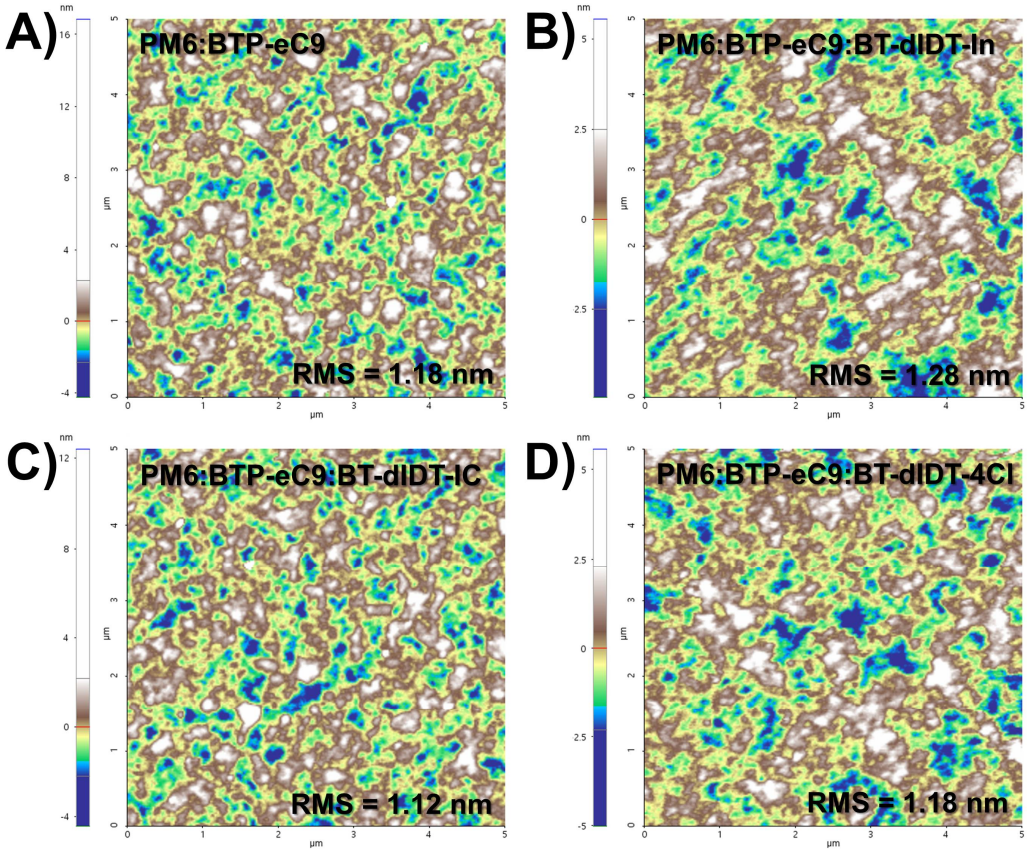

Figure 5. (**A**–**D**) AFM height images (5 × 5 μm) of optimized ternary blends based on (**A**) PM6:BTP-eC9 = 1:1.2, (**B**) PM6:BTP-eC9:**BT-dIDT-In** = 1:1.1:0.1, (**C**) PM6:BTP-eC9:**BT-dIDT-IC** = 1:1.1:0.1, and (**D**) PM6:BTP-eC9:**BT-dIDT-4Cl** = 1:1.1:0.1.

3.6. Eco-Friendly Solvent-Based Photovoltaic Performance

All long-conjugated NFAs with stretched S-shape curvatures exhibit significantly greater solubility in common organic solvents compared to the Y-shaped BTP-eC9. Simple

solubility tests revealed that all long-conjugated NFAs can dissolve in tetrahydrofuran (THF) at concentrations exceeding 10 mg/mL without the need for heating. In contrast, BTP-eC9 exhibited a limited solubility at the same concentration in THF. The high solubility of long-conjugated NFAs can be attributed to the presence of eight sp^3 carbon-bridged hexyl phenyl side chains [20], which create sufficient geometric space for interactions with organic solvent molecules. Despite the presence of steric hindrance caused by the N-alkyl chains in the BTP-eC9 core, which exhibit a tilting angle of 17.5°, as illustrated in the side view (Figure 1D), eco-friendly solvents have difficulty surrounding and solvating the BTP-eC9 molecule.

Given the potential of long-conjugated NFAs in eco-friendly applications, it is desirable to investigate the photovoltaic performance of ternary OSC devices processed using eco-friendly solvents. As shown in Figure S16, all devices were fabricated utilizing the eco-friendly solvent XY. The binary device based on the PM6:BTP-eC9 blend showed a PCE of 16.21%, which is comparable to that of the corresponding device using the halogenated solvent CF (16.39%). Notably, long-conjugated NFA-based ternary devices incorporating **BT-dIDT-IC** and **BT-dIDT-4Cl** exhibited higher PCEs of 16.45% and 16.84%, respectively. Notably, the highest PCE observed with the **BT-dIDT-4Cl**-based ternary device can be attributed to a reduced E_{loss} value of 0.471 eV, compared to 0.484 eV in the control device. More importantly, the photovoltaic performance of the **BT-dIDT-4Cl**-based ternary device approaches 17%, which is comparable to the high-performance eco-friendly solvent-processed OSCs reported in the literature [16,17,19,25,42,43]. Detailed photovoltaic parameters are summarized in Table S8. A summary of recent progress in organic solar cells (OSCs) processed using eco-friendly solvents which have achieved power conversion efficiencies (PCEs) exceeding 16% is presented in Table S9 for a better understanding. These results provide bright insights into the applications of eco-friendly processed OSCs.

4. Conclusions

In summary, we designed and synthesized three A-D-A′-D-A-type long-conjugated NFAs, namely **BT-dIDT-In**, **BT-dIDT-IC**, and **BT-dIDT-4Cl**, by incorporating various EWGs (In, IC, and 4Cl units) into the BT-dIDT core. All NFAs have a stretched S-shape curvature with L_x values greater than 40 Å, and they exhibit distinct optical and electrochemical properties, as well as variations in their crystallinity, which are influenced by the modification of their EWGs. Only **BT-dIDT-IC** and **BT-dIDT-4Cl** demonstrated significant potential for high-efficiency ternary organic solar cells (OSCs) based on the PM6:BTP-eC9 (ref.) blend. As a result, when processed with CF solutions, the **BT-dIDT-IC** and **BT-dIDT-4Cl**-incorporated ternary OSCs yielded higher PCEs of 16.73% and 16.63%, respectively, compared to that of the reference device (16.39%). Additionally, when processed with eco-friendly XY solvent solutions, the **BT-dIDT-IC** and **BT-dIDT-4Cl**-incorporated ternary OSCs yielded higher PCEs of 16.45% and 16.84%, respectively, compared to that of the reference device (16.21%). From the perspective of structure–property relationships, we systematically investigated and discussed various properties of these devices, including their molecular design and synthesis, thermal properties, computational simulations, optical and electrochemical properties, crystallinity and orientation properties, and morphological properties. This study offers valuable insights for the development of NFAs in the context of efficient and environmentally friendly OSCs.

Supplementary Materials: The following supporting information can be downloaded at https://www.mdpi.com/article/10.3390/su17020512/s1. Scheme S1: Synthetic scheme of long-conjugated NFAs: BT-dIDT-In, BT-dIDT-IC, and BT-dIDT-4Cl; Figure S1: ^{1}H NMR spectrum of compound M1 in $CDCl_3$; Figure S2: ^{1}H NMR spectrum of long-conjugated NFA BT-dIDT-In in $CDCl_3$; Figure S3: MALDI-TOF spectrum of long-conjugated NFA BT-dIDT-In; Figure S4: ^{1}H NMR spectrum of

long-conjugated NFA BT-dIDT-IC in $CDCl_3$; Figure S5: MALDI-TOF spectrum of long-conjugated NFA BT-dIDT-IC; Figure S6: ^{1}H NMR spectrum of long-conjugated NFA BT-dIDT-4Cl in $CDCl_3$; Figure S7: MALDI-TOF spectrum of long-conjugated NFA BT-dIDT-4Cl; Figure S8: TGA curves of long-conjugated NFAs: BT-dIDT-In, BT-dIDT-IC, and BT-dIDT-4Cl; Figure S9: DSC curves of long-conjugated NFAs: BT-dIDT-In, BT-dIDT-IC, and BT-dIDT-4Cl; Figure S10: Normalized potential energy scans as a function of the dihedral angles (C2-C1-C12-C14) of the model compound BT-dIDT; Figure S11: DFT calculation results of the optimized geometries for the model compound PM6 (stable form) (repeating unit, n = 2): (a) top and (b) side views (dipole moment), (c) ESP surface, and (d) LUMO and (e) HOMO energy levels; Figure S12: Molar absorption coefficients of long-conjugated NFAs in the CF solutions: BT-dIDT-In, BT-dIDT-IC, and BT-dIDT-4Cl; Figure S13: Relative PL spectra of optimized binary OSCs based on PM6:NFA (BT-dIDT-In, BT-dIDT-IC, and BT-dIDT-4Cl) = 1:1, processed with CB (0.5 vol% DIO)—the samples were excited at 530 nm; Figure S14: Relative PL spectra of optimized ternary OSCs based on PM6:BTP-eC9 = 1:1.2 (ref.) and PM6:BTP-eC9:NFA (BT-dIDT-In, BT-dIDT-IC, and BT-dIDT-4Cl) = 1:1.1:0.1, processed with CF (0.5 vol% DIO)—the samples were excited at 530 nm 630 nm, respectively; Figure S15: SCLC curves of optimized ternary OSCs based on PM6:BTP-eC9 = 1:1.2 (ref.) and PM6:BTP-eC9:NFA (BT-dIDT-In, BT-dIDT-IC, and BT-dIDT-4Cl) = 1:1.1:0.1, processed with CF (0.5 vol% DIO): (a) electron- and (b) hole-only devices; Figure S16: $J-V$ and EQE curves of the eco-friendly solvent (*o*-xylene (XY) (0.3 vol% DIO))-processed OSCs based on PM6:BTP-eC9 = 1:1.2, PM6:BTP-eC9:BT-dIDT-IC = 1:1.1:0.1 and PM6:BTP-eC9:BT-dIDT-4Cl; Table S1: DFT calculation parameters of the optimized geometries for model compounds: BT-dIDT-In, BT-dIDT-IC, BT-dITC-4Cl, BTP-eC9, and PM6 (n = 2); Table S2: Optical and electrochemical properties of PM6 and BTP-eC9; Table S3: PL quenching rates and energy level offsets of optimized binary OSCs based on PM6:NFA (BT-dIDT-In, BT-dIDT-IC, and BT-dIDT-4Cl) = 1:1, processed with CB (0.5 vol% DIO)—the samples were excited at 530 nm; Table S4: PL quenching rates and energy level offsets of optimized ternary OSCs based on PM6:BTP-eC9 = 1:1.2 (ref.) and PM6:BTP-eC9:NFA (BT-dIDT-In, BT-dIDT-IC, and BT-dIDT-4Cl) = 1:1.1:0.1, processed with CF (0.5 vol% DIO)—the samples were excited at 530 nm and 630 nm, respectively; Table S5: Charge-carrier mobility results of optimized ternary OSCs based on PM6:BTP-eC9 = 1:1.2 (ref.) and PM6:BTP-eC9:NFAs (BT-dIDT-In, BT-dIDT-IC, and BT-dIDT-4Cl) = 1:1:0.1, processed with CF (0.5 vol% DIO)—electron- and hole-only devices; Table S6: 2D-GIWAXS results of neat films based on PM6, BT-dIDT-In, BT-dIDT-IC, BT-dIDT-4Cl, and BTP-eC9: (100) and (010) relevant parameters are extracted from the out-of-plane (OOP) directions, respectively; Table S7: 2D-GIWAXS results of optimized ternary based on PM6:BTP-eC9 = 1:1.2 (ref.) and PM6:BTP-eC9:NFAs (BT-dIDT-In, BT-dIDT-IC, and BT-dIDT-4Cl) = 1:1:0.1, processed with CF (0.5 vol% DIO): (100) and (010) relevant parameters are extracted from the in-plane (IP) and out-of-plane (OOP) directions, respectively; Table S8: Photovoltaic performance of the eco-friendly solvent (XY (0.3 vol% DIO))-processed OSCs based on PM6:BTP-eC9 = 1:1.2, PM6:BTP-eC9:BT-dIDT-IC = 1:1.1:0.1 and PM6:BTP-eC9:BT-dIDT-4Cl; Table S9: Summary of the recent progress of OSCs processed from eco-friendly solvents with PCEs of over 16%.

Author Contributions: Conceptualization, S.J.J.; methodology, S.J.J.; software, S.J.J.; validation, S.J.J., N.G.Y. and D.K.M.; formal analysis, S.J.J.; investigation, S.J.J.; data curation, S.J.J.; writing—original draft preparation, S.J.J.; writing—review and editing, S.J.J.; visualization, S.J.J.; resources, D.K.M.; supervision, D.K.M.; project administration, D.K.M.; funding acquisition, D.K.M. All authors have read and agreed to the published version of the manuscript.

Funding: This paper was funded by the part of Konkuk University's research support program for its faculty on sabbatical leave in 2022. This work was supported by the Commercializations Promotion Agency for R&D Outcomes (COMPA) grant funded by the Korea government (MSIT) (No. RS-2023-00304788). This work was supported in part by Human Resources Development Program of the Korea Institute of Energy Technology Evaluation and Planning (KETEP) grant funded by the Ministry of Trade, Industry and Energy, Republic of Korea (No. RS-2023-00237035).

Institutional Review Board Statement: Not applicable.

Informed Consent Statement: Not applicable.

Data Availability Statement: All the data are available within this manuscript.

Acknowledgments: This paper was written as part of Konkuk University's research support program for its faculty on sabbatical leave in 2022. This work was supported by a Commercializations Promotion Agency for R&D Outcomes (COMPA) grant funded by the Korea government (MSIT) (No. RS-2023-00304788). This work was supported in part by a Human Resources Development Program of the Korea Institute of Energy Technology Evaluation and Planning (KETEP) grant funded by the Ministry of Trade, Industry and Energy, Republic of Korea (No. RS-2023-00237035).

Conflicts of Interest: The authors declare no conflicts of interest.

References

1. Brunetti, F.; Operamolla, A.; Castro-Hermosa, S.; Lucarelli, G.; Manca, V.; Farinola, G.M.; Brown, T.M. Printed Solar Cells and Energy Storage Devices on Paper Substrates. *Adv. Funct. Mater.* **2019**, *29*, 1806798. [CrossRef]
2. Meddeb, H.; Götz-Köhler, M.; Neugebohrn, N.; Banik, U.; Osterthun, N.; Sergeev, O.; Berends, D.; Lattyak, C.; Gehrke, K.; Vehse, M. Tunable Photovoltaics: Adapting Solar Cell Technologies to Versatile Applications. *Adv. Energy Mater.* **2022**, *12*, 2200713. [CrossRef]
3. Zhou, Z.; Yuan, Z.; Yin, Z.; Xue, Q.; Li, N.; Huang, F. Progress of Semitransparent Emerging Photovoltaics for Building Integrated Applications. *Green Energy Environ.* **2024**, *9*, 992–1015. [CrossRef]
4. KISTEP. Available online: https://www.kistep.re.kr/boardDownload.es?bid=0031&list_no=93860&seq=1 (accessed on 14 November 2024).
5. Zhu, L.; Zhang, M.; Zhou, Z.; Zhong, W.; Hao, T.; Xu, S.; Zeng, R.; Zhuang, J.; Xue, X.; Jing, H.; et al. Progress of Organic Photovoltaics towards 20% Efficiency. *Nat. Rev. Electr. Eng.* **2024**, *1*, 581–596. [CrossRef]
6. Wei, N.; Chen, J.; Cheng, Y.; Bian, Z.; Liu, W.; Song, H.; Guo, Y.; Zhang, W.; Liu, Y.; Lu, H.; et al. Constructing Multiscale Fibrous Morphology to Achieve 20% Efficiency Organic Solar Cells by Mixing High and Low Molecular Weight D18. *Adv. Mater.* **2024**, *36*, 2408934. [CrossRef] [PubMed]
7. Chen, Z.; Ge, J.; Song, W.; Tong, X.; Liu, H.; Yu, X.; Li, J.; Shi, J.; Xie, L.; Han, C.; et al. 20.2% Efficiency Organic Photovoltaics Employing a π-Extension Quinoxaline-Based Acceptor with Ordered Arrangement. *Adv. Mater.* **2024**, *36*, 2406690. [CrossRef]
8. Chen, C.; Wang, L.; Xia, W.; Qiu, K.; Guo, C.; Gan, Z.; Zhou, J.; Sun, Y.; Liu, D.; Li, W.; et al. Molecular Interaction Induced Dual Fibrils towards Organic Solar Cells with Certified Efficiency over 20%. *Nat. Commun.* **2024**, *15*, 6865. [CrossRef] [PubMed]
9. Guan, S.; Li, Y.; Xu, C.; Yin, N.; Xu, C.; Wang, C.; Wang, M.; Xu, Y.; Chen, Q.; Wang, D.; et al. Self-Assembled Interlayer Enables High-Performance Organic Photovoltaics with Power Conversion Efficiency Exceeding 20%. *Adv. Mater.* **2024**, *36*, 2400342. [CrossRef]
10. Zhu, L.; Zhang, M.; Zhou, G.; Wang, Z.; Zhong, W.; Zhuang, J.; Zhou, Z.; Gao, X.; Kan, L.; Hao, B.; et al. Achieving 20.8% Organic Solar Cells via Additive-Assisted Layer-by-Layer Fabrication with Bulk p-i-n Structure and Improved Optical Management. *Joule* **2024**, *8*, 3153–3168. [CrossRef]
11. Wang, W.; Cui, Y.; Zhang, T.; Bi, P.; Wang, J.; Yang, S.; Wang, J.; Zhang, S.; Hou, J. High-Performance Organic Photovoltaic Cells under Indoor Lighting Enabled by Suppressing Energetic Disorders. *Joule* **2023**, *7*, 1067–1079. [CrossRef]
12. Wang, W.; Cui, Y.; Yu, Y.; Wang, J.; Wang, C.; Hou, H.; Kang, Q.; Wang, H.; Chen, S.; Zhang, S.; et al. Indoor Organic Photovoltaic Module with 30.6% Efficiency for Efficient Wireless Power Transfer. *Nano Energy* **2024**, *128*, 109893. [CrossRef]
13. Jeon, S.J.; Kim, Y.C.; Kim, J.Y.; Kim, J.H.; Yang, N.G.; Lee, Y.J.; Lee, H.S.; Kim, Y.H.; Kim, G.W.; Jang, E.M.; et al. Molecular Design of Cost-Effective Donor Polymers with High Visible Transmission for Eco-Friendly and Efficient Semitransparent Organic Solar Cells. *Chem. Eng. J.* **2023**, *472*, 144850. [CrossRef]
14. Basu, R.; Gumpert, F.; Lohbreier, J.; Morin, P.O.; Vohra, V.; Liu, Y.; Zhou, Y.; Brabec, C.J.; Egelhaaf, H.J.; Distler, A. Large-Area Organic Photovoltaic Modules with 14.5% Certified World Record Efficiency. *Joule* **2024**, *8*, 970–978. [CrossRef]
15. Xie, C.; Zeng, X.; Li, C.; Sun, X.; Liang, S.; Huang, H.; Deng, B.; Wen, X.; Zhang, G.; You, P.; et al. Water-Based Layer-by-Layer Processing Enables 19% Efficient Binary Organic Solar Cells with Minimized Thickness Sensitivity. *Energy Environ. Sci.* **2024**, *17*, 2441–2452. [CrossRef]
16. Dong, S.; Jia, T.; Zhang, K.; Jing, J.; Huang, F. Single-Component Non-Halogen Solvent-Processed High-Performance Organic Solar Cell Module with Efficiency over 14%. *Joule* **2020**, *4*, 2004–2016. [CrossRef]
17. Jeon, S.J.; Yang, N.G.; Kim, J.Y.; Kim, Y.C.; Lee, H.S.; Moon, D.K. A 3-Fluoropyridine Manipulating the Aggregation and Fibril Network of Donor Polymers for Eco-Friendly Solution-Processed Versatile Organic Solar Cells. *Small* **2023**, *19*, 2301803. [CrossRef]
18. Sun, R.; Yuan, X.; Yang, X.; Wu, Y.; Shao, Y.; Wu, X.; Brabec, C.J.; Min, J. Cost-Efficient Recycling of Organic Photovoltaic Devices. *Joule* **2024**, *8*, 2523–2538. [CrossRef]

19. Zhang, R.; Chen, H.; Wang, T.; Kobera, L.; He, L.; Huang, Y.; Ding, J.; Zhang, B.; Khasbaatar, A.; Nanayakkara, S.; et al. Equally High Efficiencies of Organic Solar Cells Processed from Different Solvents Reveal Key Factors for Morphology Control. *Nat. Energy* **2024**. [CrossRef]
20. Kim, M.; Ryu, S.U.; Park, S.A.; Pu, Y.J.; Park, T. Designs and Understanding of Small Molecule-Based Non-Fullerene Acceptors for Realizing Commercially Viable Organic Photovoltaics. *Chem. Sci.* **2021**, *12*, 14004–14023. [CrossRef] [PubMed]
21. Nie, Q.; Tang, A.; Guo, Q.; Zhou, E. Benzothiadiazole-Based Non-Fullerene Acceptors. *Nano Energy* **2021**, *87*, 106174. [CrossRef]
22. Chang, Q.; Chen, H.; Yuan, J.; Hu, Y.; Hai, J.; Liu, W.; Cai, F.; Hong, J.; Xiao, X.; Zou, Y. Diflurobenzothiadiazole Core-Based Noncovalently Fused Small Molecule Acceptor Exhibiting over 12% Efficiency and High Fill Factor. *J. Energy Chem.* **2020**, *51*, 7–13. [CrossRef]
23. Zhang, M.; Zeng, M.; Chen, H.; Li, L.; Zhao, B.; Tan, S. A2-D-A1-D-A2-Type Small Molecule Acceptors Incorporated with Electron-Deficient Core for Non-Fullerene Organic Solar Cells. *Sol. Energy* **2020**, *197*, 511–518. [CrossRef]
24. Jeon, S.J.; Kim, Y.H.; Kim, I.N.; Yang, N.G.; Yun, J.H.; Moon, D.K. Utilizing 3,4-Ethylenedioxythiophene (EDOT)-Bridged Non-Fullerene Acceptors for Efficient Organic Solar Cells. *J. Energy Chem.* **2022**, *65*, 194–204. [CrossRef]
25. Xue, Y.J.; Lai, Z.Y.; Lu, H.C.; Hong, J.C.; Tsai, C.L.; Huang, C.L.; Huang, K.H.; Lu, C.F.; Lai, Y.Y.; Hsu, C.S.; et al. Unraveling the Structure-Property-Performance Relationships of Fused-Ring Nonfullerene Acceptors: Toward a C-Shaped Ortho-Benzodipyrrole-Based Acceptor for Highly Efficient Organic Photovoltaics. *J. Am. Chem. Soc.* **2024**, *146*, 833–848. [CrossRef]
26. Bai, Y.; Hong, L.; Dou, Y.; Zhu, S.; Tang, H.; Liu, D.; Cao, Y.; Chen, J.; Chen, S.; Shao, L.; et al. C-Shape or S-Shape? The Molecular Geometry Control of Fused-Ring Nonfullerene Acceptors for Lower Energy Loss in Organic Solar Cells. *ACS Energy Lett.* **2024**, *9*, 1786–1795. [CrossRef]
27. Wang, Y.; Zhang, S.; Wang, J.; Ren, J.; Qiao, J.; Chen, Z.; Yu, Y.; Hao, X.T.; Hou, J. Optimizing Phase Separation and Vertical Distribution via Molecular Design and Ternary Strategy for Organic Solar Cells with 19.5% Efficiency. *ACS Energy Lett.* **2024**, *9*, 2420–2427. [CrossRef]
28. Kim, I.N.; Jeon, S.J.; Kim, Y.H.; Lee, H.S.; Han, Y.W.; Yang, N.G.; Hong, D.H.; Jung, C.H.; Moon, D.K. Synthesis of 3,4-Dimethoxythiophene Spacer-Based Non-Fullerene Acceptors for Efficient Organic Solar Cells. *Synth. Met.* **2021**, *280*, 116880. [CrossRef]
29. Qin, Y.; Chen, H.; Yao, J.; Zhou, Y.; Cho, Y.; Zhu, Y.; Qiu, B.; Ju, C.W.; Zhang, Z.G.; He, F.; et al. Silicon and Oxygen Synergistic Effects for the Discovery of New High-Performance Nonfullerene Acceptors. *Nat. Commun.* **2020**, *11*, 5814. [CrossRef]
30. Cho, H.W.; An, N.G.; Park, S.Y.; Shin, Y.S.; Lee, W.; Kim, J.Y.; Song, S. Thermally Durable Nonfullerene Acceptor with Nonplanar Conjugated Backbone for High-Performance Organic Solar Cells. *Adv. Energy Mater.* **2020**, *10*, 1903585. [CrossRef]
31. Gao, W.; Liu, T.; Zhong, C.; Zhang, G.; Zhang, Y.; Ming, R.; Zhang, L.; Xin, J.; Wu, K.; Guo, Y.; et al. Asymmetrical Small Molecule Acceptor Enabling Nonfullerene Polymer Solar Cell with Fill Factor Approaching 79%. *ACS Energy Lett.* **2018**, *3*, 1760–1768. [CrossRef]
32. Deng, M.; Xu, X.; Duan, Y.; Yu, L.; Li, R.; Peng, Q. Y-Type Non-Fullerene Acceptors with Outer Branched Side Chains and Inner Cyclohexane Side Chains for 19.36% Efficiency Polymer Solar Cells. *Adv. Mater.* **2023**, *35*, 2210760. [CrossRef] [PubMed]
33. Chen, C.; Wang, L.; Sun, Y.; Fu, Y.; Guo, C.; Zhou, B.; Gan, Z.; Liu, D.; Li, W.; Wang, T. Realizing an Unprecedented Fill Factor of 82.2% in Ternary Organic Solar Cells via Co-Crystallization of Non-Fullerene Acceptors. *Adv. Funct. Mater.* **2023**, *33*, 2305765. [CrossRef]
34. Kim, H.S.; Song, C.E.; Ha, J.W.; Lee, S.; Rasool, S.; Lee, H.K.; Shin, W.S.; Hwang, D.H. Synthesis of ITIC Derivatives with Extended π-Conjugation as Non-Fullerene Acceptors for Organic Solar Cells. *ACS Appl. Mater. Interfaces* **2019**, *11*, 47121–47130. [CrossRef] [PubMed]
35. Kim, H.S.; Rasool, S.; Shin, W.S.; Song, C.E.; Hwang, D.H. Alkylated Indacenodithiophene-Based Non-Fullerene Acceptors with Extended π-Conjugation for High-Performance Large-Area Organic Solar Cells. *ACS Appl. Mater. Interfaces* **2020**, *12*, 50638–50647. [CrossRef]
36. Cui, Y.; Yao, H.; Zhang, J.; Xian, K.; Zhang, T.; Hong, L.; Wang, Y.; Xu, Y.; Ma, K.; An, C.; et al. Single-Junction Organic Photovoltaic Cells with Approaching 18% Efficiency. *Adv. Mater.* **2020**, *32*, 1908205. [CrossRef] [PubMed]
37. Cui, Y.; Yao, H.; Hong, L.; Zhang, T.; Tang, Y.; Lin, B.; Xian, K.; Gao, B.; An, C.; Bi, P.; et al. Organic Photovoltaic Cell with 17% Efficiency and Superior Processability. *Natl. Sci. Rev.* **2021**, *7*, 1239–1246. [CrossRef] [PubMed]
38. Shang, A.; Luo, S.; Zhang, J.; Zhao, H.; Xia, X.; Pan, M.; Li, C.; Chen, Y.; Yi, J.; Lu, X.; et al. Over 18% Binary Organic Solar Cells Enabled by Isomerization of Non-Fullerene Acceptors with Alkylthiophene Side Chains. *Sci. China Chem.* **2022**, *65*, 1758–1766. [CrossRef]
39. Jasiūnas, R.; Zhang, H.; Gelžinis, A.; Chmeliov, J.; Franckevičius, M.; Gao, F.; Gulbinas, V. Interplay between Charge Separation and Hole Back Transfer Determines the Efficiency of Non-Fullerene Organic Solar Cells with Low Energy Level Offset. *Org. Electron.* **2022**, *108*, 106601. [CrossRef]

40. Xu, J.; Jo, S.B.; Chen, X.; Zhou, G.; Zhang, M.; Shi, X.; Lin, F.; Zhu, L.; Hao, T.; Gao, K.; et al. The Molecular Ordering and Double-Channel Carrier Generation of Nonfullerene Photovoltaics within Multi-Length-Scale Morphology. *Adv. Mater.* **2022**, *34*, 2108317. [CrossRef]
41. Xiao, B.; Zhang, M.; Yan, J.; Luo, G.; Gao, K.; Liu, J.; You, Q.; Wang, H.B.; Gao, C.; Zhao, B.; et al. High Efficiency Organic Solar Cells Based on Amorphous Electron-Donating Polymer and Modified Fullerene Acceptor. *Nano Energy* **2017**, *39*, 478–488. [CrossRef]
42. Gao, S.; Zhang, Y.; Jeong, S.; Zhou, X.; Xu, H.; Xu, S.; Chen, D.; Liu, W.; Yang, C.; Meng, S.; et al. Ameliorated Trap Density and Energetic Disorder via a Strengthened Intermolecular Interaction Strategy to Construct Efficient Non-Halogenated Organic Solar Cells. *Energy Environ. Sci.* **2024**, *17*, 5542–5551. [CrossRef]
43. Yu, Y.Y.; Shih, K.Y.; Peng, Y.C.; Chiu, Y.C.; Kuo, C.C.; Yang, C.C.; Chen, C.P. High-Efficiency Organic Photovoltaic Cells Processed Using a Non-Halogen Solvent. *Mater. Chem. Phys.* **2022**, *282*, 125971. [CrossRef]